

# All-dielectric subwavelength metasurface focusing lens

Paul R. West,<sup>1</sup> James L. Stewart,<sup>1</sup> Alexander V. Kildishev,<sup>1,\*</sup> Vladimir M. Shalaev,<sup>1</sup>  
Vladimir V. Shkunov,<sup>2</sup> Friedrich Strohkendl,<sup>2</sup> Yuri A. Zakharenkov,<sup>2</sup> Robert K.  
Dodds,<sup>2</sup> and Robert Byren<sup>2</sup>

<sup>1</sup>*School of Electrical and Computer Engineering and Birck Nanotechnology Center, Purdue University, West Lafayette, IN 47907, USA*

<sup>2</sup>*Raytheon Space and Airborne Systems, 2000 East El Segundo Blvd, PO Box 902, El Segundo, CA 90245, USA*  
*\*kildishev@purdue.edu*

**Abstract:** We have proposed, designed, manufactured and tested low loss dielectric micro-lenses for infrared (IR) radiation based on a dielectric metamaterial layer. This metamaterial layer was created by patterning a dielectric surface and etching to sub-micron depths. For a proof-of-concept lens demonstration, we have chosen a fine patterned array of nano-pillars with variable diameters. Gradient index (GRIN) properties were achieved by engineering the nano-pattern characteristics across the lens, so that the effective optical density of the dielectric metamaterial layer peaks around the lens center, and gradually drops at the lens periphery. A set of lens designs with reduced reflection and tailorable phase gradients have been developed and tested, demonstrating focal distances of a few hundred microns, beam area contraction ratio up to three, and insertion losses as low as 11%.

©2014 Optical Society of America

**OCIS codes:** (240.5420) Polaritons; (050.1965) Diffractive lenses; (220.1770) Concentrators; (050.5080) Phase shift; (050.6624) Subwavelength structures; (160.3918) Metamaterials.

---

## References and links

1. W. Stork, N. Streibl, H. Haidner, and P. Kipfer, "Artificial distributed-index media fabricated by zero-order gratings," *Opt. Lett.* **16**(24), 1921–1923 (1991).
2. M. W. Farn, "Binary gratings with increased efficiency," *Appl. Opt.* **31**(22), 4453–4458 (1992).
3. H. Haidner, P. Kipfer, J. Sheridan, J. Schwider, N. Streibl, M. Collischon, J. Hutfless, and M. März, "Diffraction gratings with rectangular grooves exceeding 80% diffraction efficiency," *Infrared Phys.* **34**(5), 467–475 (1993).
4. F. T. Chen and H. G. Craighead, "Diffractive phase elements based on two-dimensional artificial dielectrics," *Opt. Lett.* **20**(2), 121–123 (1995).
5. F. T. Chen and H. G. Craighead, "Diffractive lens fabricated with mostly zeroth-order gratings," *Opt. Lett.* **21**(3), 177–179 (1996).
6. S. Astilean, P. Lalanne, P. Chavel, E. Cambril, and H. Launois, "High-efficiency subwavelength diffractive element patterned in a high-refractive-index material for 633 nm," *Opt. Lett.* **23**(7), 552–554 (1998).
7. M. S. Lee, P. Lalanne, J. C. Rodier, and E. Cambril, "Wide-field-angle behavior of blazed-binary gratings in the resonance domain," *Opt. Lett.* **25**(23), 1690–1692 (2000).
8. S. Wilson and M. Hutley, "The optical properties of 'moth eye' antireflection surfaces," *J. Mod. Opt.* **29**(7), 993–1009 (1982).
9. P. Lalanne, S. Astilean, P. Chavel, E. Cambril, and H. Launois, "Design and fabrication of blazed binary diffractive elements with sampling periods smaller than the structural cutoff," *J. Opt. Soc. Am. A* **16**(5), 1143–1156 (1999).
10. N. Yu, P. Genevet, M. A. Kats, F. Aieta, J. P. Tetienne, F. Capasso, and Z. Gaburro, "Light propagation with phase discontinuities: generalized laws of reflection and refraction," *Science* **334**(6054), 333–337 (2011).
11. E. B. Kley, W. Freese, T. Kampfe, A. Tunnermann, U. D. Zeitner, D. Michaelis, and M. Erdmann, "Large-scale application of binary subwavelength structures," in 2009 IEEE/LEOS International Conference on Optical MEMS and Nanophotonics (2009), pp. 148–149.
12. M.-S. L. Lee, S. Bansropun, O. Huet, S. Cassette, B. Loiseaux, A. P. Wood, C. Sauvan, and P. Lalanne, "Subwavelength structures for broadband diffractive optics," *Proc. SPIE* **6029**, 602919 (2006).
13. C. Sauvan, P. Lalanne, and M. S. Lee, "Broadband blazing with artificial dielectrics," *Opt. Lett.* **29**(14), 1593–1595 (2004).

14. C. Ribot, M. Lee, S. Collin, S. Bansropun, P. Plouhinec, D. Thenot, S. Casette, B. Loiseaux, and P. Lalanne, "Broadband and efficient diffraction," *Adv. Opt. Mater.* **1**(7), 489–493 (2013).
15. M. Kuittinen, J. Turunen, and P. Vahimaa, "Rigorous analysis and optimization of subwavelength-structured binary dielectric beam deflector gratings," *J. Mod. Opt.* **45**(1), 133–142 (1998).
16. P. Lalanne, J. Rodier, P. Chavel, E. Cambriil, A. Talneau, and Y. Chen, "Applications of index-gradient artificial dielectrics," *SPIE Proc.* 1–7 (2003).
17. M. Lee, P. Lalanne, A. Wood, and C. Sauvan, WIPO Patent No. 2005038501. Geneva, Switzerland: World Intellectual Property Organization (2005).
18. P. Lalanne and M. Hutley, "Artificial media optical properties – subwavelength scale," in *Encyclopedia of Optical Engineering*, R. Driggers, ed. (Marcel Dekker), Vol. 1, 62–71 (2003).
19. J. Feng and Z. Zhou, "Polarization beam splitter using a binary blazed grating coupler," *Opt. Lett.* **32**(12), 1662–1664 (2007).
20. J. Feng and Z. Zhou, "High-efficiency compact grating coupler for integrated optical circuits," *Proc. SPIE* **6351**, 65311H (2006).
21. P. Lalanne, "Waveguiding in blazed-binary diffractive elements," *J. Opt. Soc. Am. A* **16**(10), 2517–2520 (1999).
22. W. Freese, T. Kämpfe, W. Rockstroh, E. B. Kley, and A. Tünnermann, "Optimized electron beam writing strategy for fabricating computer-generated holograms based on an effective medium approach," *Opt. Express* **19**(9), 8684–8692 (2011).
23. W. Freese, T. Kämpfe, E.-B. Kley, and A. Tünnermann, "Design and fabrication of a highly off-axis binary multi-phase level computer-generated hologram based on an effective medium approach," *Proc. SPIE* **7927**(792710), 792710, (2011).
24. W. Yu, K. Takahara, T. Konishi, T. Yotsuya, and Y. Ichioka, "Fabrication of multilevel phase computer-generated hologram elements based on effective medium theory," *Appl. Opt.* **39**(20), 3531–3536 (2000).
25. V. Raulot, B. Serio, P. Gérard, P. Twardowski, and P. Meyrueis, "Modeling of a diffractive micro-lens by an effective medium method," *Proc. SPIE Proc. SPIE* **7716**, 77162J–77162J, (2010).
26. B. Kleemann, *U.S. Patent No. 7,262,915*. Washington, DC: U.S. Patent and Trademark Office. (2007).
27. M. Lee, P. Lalanne, J. Rodier, P. Chavel, E. Cambriil, and Y. Chen, "Imaging with blazed-binary diffractive elements," *J. Opt. A* **4**(5), S119–S124 (2002).
28. M. Lee, P. Lalanne, P. Chavel, and E. Cambriil, "Imaging with blazed-binary diffractive elements," *Proc. SPIE* **4438**, 62–68 (2001).
29. D. Fattal, J. Li, Z. Peng, M. Fiorentino, and R. G. Beausoleil, "A Silicon Lens for Integrated Free-Space Optics," in *Advanced Photonics* (Optical Society of America, Toronto, 2011), p. ITuD2.
30. M. Lee, P. Pichon, C. Sauvan, J. Rodier, P. Lalanne, M. Hutley, and Y. Chen, "Transmission blazed-binary gratings for visible light operation: performances and interferometric characterization," *J. Opt. A* **5**(5), S244–S249 (2003).
31. D. Lin, P. Fan, E. Hasman, and M. L. Brongersma, "Dielectric gradient metasurface optical elements," *Science* **345**(6194), 298–302 (2014).

---

## 1. Introduction

Flat and compact micro-lens arrays can be used for many applications including imaging systems, displays, and detectors. In contrast to conventional curved lenses and lens arrays, dielectric meta-surface lenses can be readily wafer-level integrated and manufactured using processes compatible with CMOS technology. These lenses can be designed to improve the effective array filling factor by being tightly mapped on a surface. Size, weight, and other packaging characteristics for optical sensors, as well as assembly cost, can be improved significantly. Making binary surface GRIN lenses as a metamaterial layer can be more efficient, compared with conventional methods of micro-lens manufacturing (such as surface profiled Fresnel lenses, geometric micro-machined lenses, or an assembly of separate discrete micro-lenses into arrays).

Planar binary surfaces with sub-wavelength patterns have been developed in the past [1–7] and used for reducing the reflection [8] from high index materials, as well as modulating the phase [9] of the transmitted wave. While this phase modulation can be accomplished using plasmonic surfaces [10], dielectric meta-surfaces have the huge advantage of reducing or even eliminating insertion losses. Strong intrinsic absorption within an operational spectral band located in the vicinity of the plasmonic resonances results in very low transmission through plasmonic meta-surfaces, at a level of a few percent at best. This makes the plasmonic approach impractical for transmission optics applications. Conversely, the sub-wavelength structures of meta-surfaces are virtually dissipation free (even near polaritonic resonances), if a transparent dielectric is used as the lens material. 440 nm was chosen.

Similar dielectric diffractive structures have been used for designing physically thin versions of various optical components, including blazed gratings [11–18], waveguide couplers [19–21], and computer generated holograms [22–24]. Flat lenses based on diffractive structures have also been proposed [17, 25, 26] and demonstrated [9,25]. For example, a TiO<sub>2</sub> blazed grating lens has been developed for a wavelength of 860 nm, with a demonstrated focal length of 400 μm [15,26]. Other similar lenses were proposed for on-axis and off-axis imaging [16,27,28]. A similar lens operating in the visible range (650nm) has been proposed using silicon pillars on an oxide substrate [29]. Although silicon is absorbing in the visible and NIR range, losses in the proposed lens are on the order of 20% at an operational wavelength of 650nm when using a transparent substrate, due to the small volume fraction of Si in the structure.

## 2. Approach

We have developed a simple design for a thin dielectric meta-surface lens that can be easily manufactured with relaxed tolerance, compared to precision diffractive structures. The objective was to create a sub-wavelength, fine-patterned meta-surface as a phase mask with a smooth radial dependence of phase increment on transmission, avoiding  $2\pi$  phase steps. Quasi-parabolic radial gradients of phase along the surface were created by slow variation of geometric parameters of the fine pattern. The meta-surface thickness is approximately one-third of the free-space wavelength ( $\lambda_0 = 1.55 \mu\text{m}$ , and height  $\approx 0.5 \mu\text{m}$ ), in our specific case. Hence, the phase mask depth variation,  $\Delta\phi \approx 2\pi\delta n(h/\lambda_0) \sim 2 \cdot \delta n \text{ rad} < 2\pi$ , across the lens area is relatively small. Therefore, the mask covers just one single central Fresnel zone of the transmitted beam, rather than multiple Fresnel zone rings with  $2\pi$  phase steps as are typical in a diffractive lens structure. As our experiments show, a mask of this type can be sufficient to reduce a laser spot diameter by a factor of about three, which can be very useful for many laser receiver, non-imaging, and optical sensing applications.

For a proof-of-concept demonstration, we selected a nano-patterned regular array of pillars etched with near vertical walls over the silicon wafer surface. The periodicity of pillar positions has been chosen to be constant over the entire lens, while the pillar diameter gradually varies from the lens center to its periphery to create spatial variations in effective refractive index of the meta-layer. To obtain a phase mask with only 0th order diffraction that minimizes scattering loss into other diffraction orders of the periodic structure, the periodicity of the pillar structures must be less than the structure cutoff scale,  $\lambda_0/n$ , where  $\lambda_0$  is the wavelength in free space, and  $n$  is the refractive index of the substrate. For the case of 1.55 μm incident light with a silicon substrate, the pillar periodicity should be less than about 445 nm (here, 440 nm was chosen). The pillars were arranged into a square symmetry lattice in the x- and y- (in-plane) directions to guarantee the same optical characteristics under both x- and y-polarization. As a first approximation, we assume that all pillars will have approximately the same height (given by the etching depth) due to the simultaneous etching of all structures.

Before fabrication, a commercial software package utilizing Finite Element Method (FEM) was used to simulate the optical properties of various structures. A parametric three-dimensional model of periodical pillar structures was simulated, and phase increments of transmission and reflection were calculated. Parametric sweeps were run over the pillar height, diameter, and wall slope to find structures exhibiting both low reflection and large phase increments. Due to practical fabrication reasons, all of the pillar heights and wall slopes were maintained constant across the entire structure in simulations, while the pillars' diameter were varied across the surface – providing the required phase distribution.

The phase of a wavefront incident on a conventional lens is modulated by the lens' curved profile resulting in lateral variations of the optical path due to glass thickness variations across the lens. Similarly, a dielectric meta-lens alters the optical path length (phase) of the transmitted light. The lens thickness is constant, and it is the effective index of the layer that

varies, as takes place for conventional gradient index (GRIN) lenses. Using pillars of different diameters while maintaining the same periodicity, the volumetric fill factor of the substrate material (vs. air) can be tailored across the meta-layer surface. Extended dynamic range of the phase variations in the transmitted light requires a large variation in the effective refractive index of the sub-wavelength thin modified layer. The dielectric metamaterial forming the desired meta-layer provides this capability.

A plane wave incident on this lens will exit the surface with the curved phase profile – characteristic of a positive focusing lens are shown in Fig. 1.

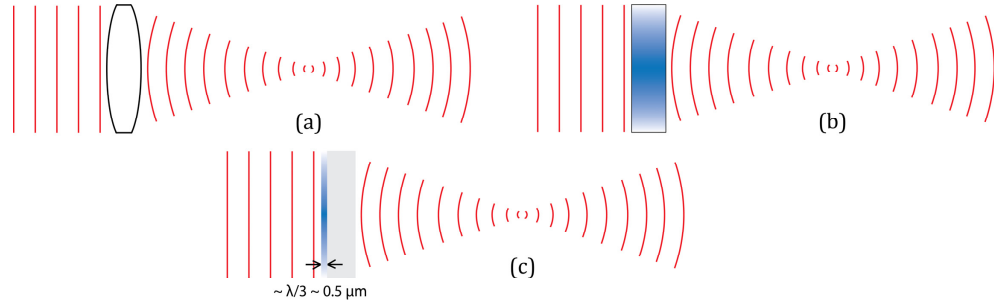


Fig. 1. Plane wave-fronts (shown in red) travelling through a conventional thick, curved lens (a), compared to a thick gradient index (GRIN) lens (b), and to a thin, flat meta-surface lens (c).

### 3. Design

Pillars with a small diameter will result in a low fill factor, mostly dominated by the air between the pillars; the effective index will approach that of air, index  $n = 1$ . Such areas of the pattern will accumulate a small leading phase, and are placed at the periphery of the lens. Thicker pillars with larger diameters result in a higher volumetric fill factor with a higher attendant effective index and these will accumulate a large lagging phase, slowing the wave-front of the incident field.

Our models show that the effective index of the actual meta-layer deviates from the simple direct proportionality to volumetric filling factor. As an example, interactions of transmitted light with localized polaritons in the nano-structures results in pushing more light into volumes occupied by the high index substrate dielectric. In general, dielectric meta-layers can be designed to provide sharper spatial phase gradients than ones anticipated from simplified fill-factor effective medium models. Fabry-Perrot type of spectral resonances created between two interfaces bordering the meta-layer should also be accounted for. In particular, transmission and reflection characteristics of the meta-layer become dependent on wavelength and on angle of incidence.

The lenses examined in this paper are each  $30 \mu\text{m} \times 30 \mu\text{m}$  in size and square-shaped. The nano-pattern for every lens consists of five concentric “belts”. The belts are formed by a discrete collection of square “tiles”, each  $3 \mu\text{m} \times 3 \mu\text{m}$  in size. The pillars’ diameter is constant over the whole surface for every tile, see Fig. 2. Thus, the belts were formed by pillars with constant diameter. We explored two designs – “square” and “rounded” lenses, both shown on the images in Fig. 2. The diameter of the pillars changes from belt to belt (see Fig. 2), and belts are arranged with thick pillars near the lens center and thin pillars towards the periphery. Discrete (as opposed to continuously varying) tiles were chosen due to their design simplicity, and practicality in optical measurements (discussed later).

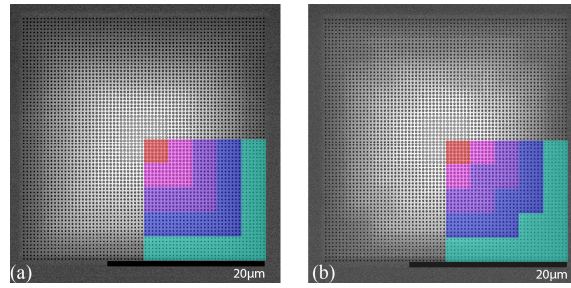


Fig. 2. Top-view of the two realizations of the lens designs: a “square” lens (left), and the “rounded” lens (right), with notched belt corners. The colored region shows the arrangement of the belts for each lens, with thick pillars near the lens center and thin pillars towards the periphery.

#### 4. Fabrication method

The pillar structures were fabricated by first patterning the circular discs used as a mask for dry etching (Fig. 3). The lithography was done using a Leica VB6 electron beam writer on a double-side-polished silicon substrate with ZEP resist. Upon lithography and development, a 45 nm thick aluminum mask was deposited, preceded by a 2 nm titanium adhesion layer via electron beam evaporation. The ZEP resist was removed via lift-off, leaving the aluminum mask on the substrate – used for etching. The etching was performed over the entire substrate, leaving behind only the small areas protected by the aluminum mask. Upon plasma etching, these aluminum circular discs leave behind cylindrical silicon pillars rising up from the flat, etched substrate. Three alternating steps of Reactive Ion Etching (RIE) and Scanning Electron Microscopy (SEM) were performed. In each step, the etching recipe was altered to ensure vertically etched sidewalls and precise etching depths. After reaching a depth of 550 nm, the aluminum mask was removed using Nanostrip, leaving behind the array of vertical silicon pillars of different diameters.

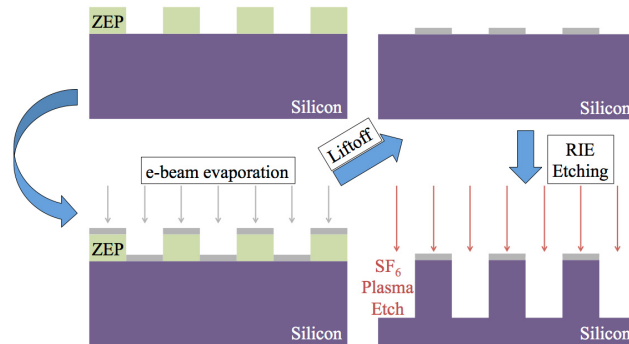


Fig. 3. Schematic showing the major steps of the fabrication process.

In total, three different combinations of five nano-patterns for every lens were selected to provide gradual variation of transmitted phase increments using preliminary modeling predictions. Altogether, 15 different nano-patterns for tiles were used to design all the lenses. SEM photos for two of the 15 of nano-patterns are shown in Fig. 4. For every combination of the belt patterns, both “square” and “rounded” lens tile geometries (see Fig. 2) were applied to design  $30\mu\text{m} \times 30\mu\text{m}$  lenses. Moreover, to reduce the risk of manufacturing accuracy, every lens design was implemented in three versions: one was patterned with an optimal pillar diameter, while another two had small deviations from the optimum, both larger and smaller values. So, in total, 6 unique lens realizations were patterned and fabricated on the same wafer.

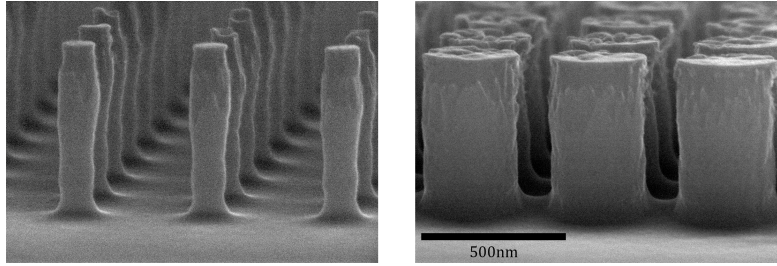


Fig. 4. Side-view of the pillar structures that modulate the phase of light passing through the lens. Pillars of large and small diameter etched to similar depths.

Along with the lenses, 15 ( $120\ \mu\text{m} \times 120\ \mu\text{m}$ ) arrays of pillars were fabricated simultaneously on the same wafer. These 15 arrays were patterned uniformly, each containing pillars with the same diameter over the entire area. These replicate the nano-patterns for all 15 elementary tiles we used for the lens designs. The additional arrays allowed independent measurements of transmission through such patterns, which were required to validate the model.

### 5. Phase increment measurements

Upon fabrication, SEM images of the 15 large ( $120\ \mu\text{m} \times 120\ \mu\text{m}$ ) arrays were monitored to measure the final dimensions of the pillars in each array. These parameters were fed into the original 3D FEM model, simulating predictions for the reflection and phase of the field passing through each uniformly patterned tile. To experimentally validate our model, the phase acquired upon crossing the pillar arrays was experimentally measured using the shearing interferometer technique setup shown in Fig. 5 and similar to previous work [30]. The incident beam spot straddled the interface between the patterned region and the bare silicon surface, so that each half of the beam experienced different phase shifts crossing the wafer. The position of the interference fringes (formed by interfering these two parts of the illuminating laser beam) were compared to fringe positions when the sample was laterally shifted so that both parts of the beam crossed the un-patterned area of the wafer. As a result, a phase increment accumulated upon passing through each pillar array was compared to the increment accumulated upon passing through the surrounding flat substrate of the same thickness.

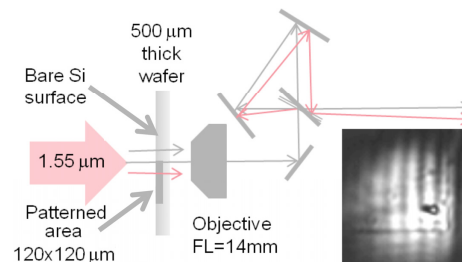


Fig. 5. Experimental optical phase measurement setup. The phase of each uniform array was measured by detecting the shift in the interference pattern created between the beam passing through the patterned and bare silicon surface.

The experimentally measured phase shift of each uniform array is shown and compared to the computer simulations in Fig. 6. We clearly see a close correspondence between the simulated and measured phase, and the simulations are well within the margin of experimental error.

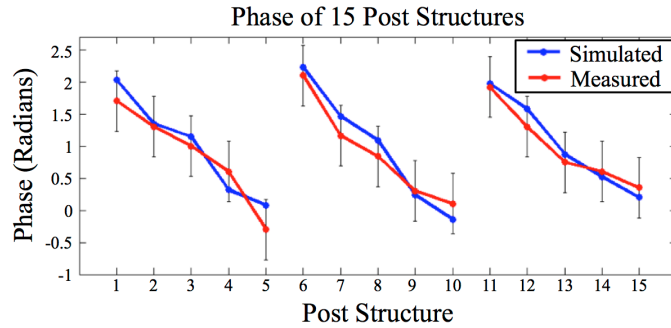


Fig. 6. Simulation (blue) and experimental measurements (red) for phase increments added by patterned meta-surfaces for the 15 pillar structures. The black error bars represent the 15% margin of error in the experimental measurements.

The arrays in the set we tested were enumerated using the following convention. Of these 15 structures, arrays 1-5 were used to form the 5 sequential concentric belts, starting from the lens center. Patterns 1-5 were used for lens design #1. Arrays 6-10, similarly, refer to the concentric belts of lens design #2. Finally, the arrays 11-15 form the concentric rings of the lens #3 design. Collectively, the gradual phase variations from belt to belt of the lens will shape the wavefront, producing the focusing behavior of the lens (as sketched in Fig. 1).

## 6. Focusing effect

Focusing properties of the meta-lenses were experimentally studied in a separate set of experiments. The surface of the silicon wafer lens was illuminated from the patterned side with a collimated 1.55  $\mu\text{m}$  laser beam, shown in Fig. 7.

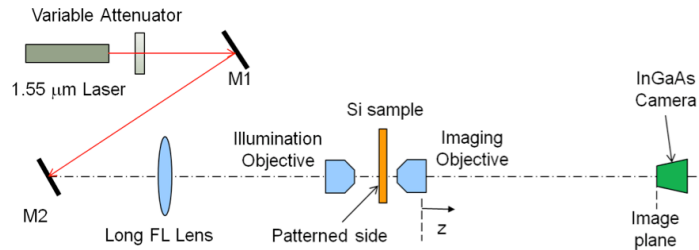


Fig. 7. Schematic of the focusing effect demonstration. The single mode radiation from an Er fiber laser was tightly focused on the Si sample surface to monitor beam diffraction behind the surface micro-lens using a simple imaging system.

The goal for this experiment was to monitor the spatial structure of the beam spot after the light had been transmitted through the lens. Different beam cross sections were imaged behind the lens with a high magnification onto an InGaAs camera (with a magnification factor of about 1:30). The evolution of the diffraction pattern (which is induced by the nano-patterned phase mask) was captured by displacing the position of the imaging plane along the z-direction. A large diameter uniform beam (that overfilled the lens), or a Gaussian beam approximately matching the size of the lenses were used. The small diameter Gaussian beam was deliberately tilted at a small angle (about  $10^\circ$ ), with respect to the normal. This tilt helped avoid interference of the transmitted light with secondary reflections from the 0.5 mm thick silicon wafer surfaces that could potentially interfere with the primary images. A microscope objective placed directly behind the silicon wafer collected light and was used for imaging. The position of the imaged cross-sections was varied in small increments by displacing the microscope objective position, or by moving the camera along the z-direction.

Figure 8 illustrates the dynamics of the focal spot evolution along the z-axis behind one of the micro-lenses. Here, the wafer was illuminated by a large beam at normal incidence. The



spatial fluctuations seen in the background of the figure are artifacts typical in coherent imaging. Imaging the wafer surface plane where the lens is located ( $z = 0$ ) provides a reasonably flat intensity profile. At a distance of about  $160\ \mu\text{m}$  behind the micro-lens (inside the wafer), the light is focused to a round spot of highest concentration. This spot is much smaller than the  $30\ \mu\text{m} \times 30\ \mu\text{m}$  size of the micro-lens (which is depicted as a yellow box in Fig. 8). The positions of the image plane have been calculated to account for refraction of the imaging light at the output Si/air interface. When shifting the image plane further into the wafer bulk, the spot size increases. The beam spreading continues more rapidly when light escapes from the Si wafer into air.

Figure 9 shows the intensity distribution at different imaging planes for the case when a  $24\ \mu\text{m}$  diameter tilted Gaussian beam illuminated the “square” micro-lens (left photo in Fig. 2). Right at the micro-lens location (i.e. at input interface of the wafer) plane, the original Gaussian profile is seen. The plane of minimal spot size (which we call the focusing plane) is shown in the middle, along with the plane one focal length behind the focusing plane, shown on the right. The plot in Fig. 9(c) compares the original Gaussian intensity profile with the profile at the focal spot. It can be seen that the lens reduces the beam spot size by nearly a factor of three – the FWHM of the incident light is decreased from  $32\ \mu\text{m}$  to  $11\ \mu\text{m}$ . The on-axis intensity increases by a factor of 1.87 in this case (compared to input beam intensity).

The photos in Fig. 9 demonstrate that along with the tightly focused spots, a halo pattern around the spots is present near the focus. The light power distributed over the halo around the spots explains why the peak intensity increase at the focal spot center is less than would be expected from just beam area reduction. The halo carries imprints of the square symmetry of the lens design, indicating that the halo is an aberration effect associated with the discrete “tiled” square lens design. Perfecting the lens design, making the phase mask deeper and the step size more gradual could increase the light intensity at the tight focal spot, as compared to intensity of the incident light, by an order of magnitude.

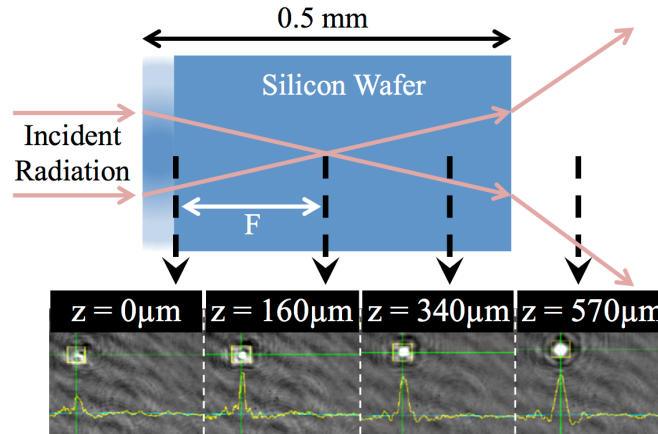


Fig. 8. Intensity profiles taken at different image planes behind the micro-lens surface measured from the input surface of the wafer. The micro-lens is strong enough to focus light inside the wafer. The yellow-color frame depicts a  $30\ \mu\text{m} \times 30\ \mu\text{m}$  box equivalent to the size of the micro-lens.

Table 1 shows examples of the optical characteristics for two different micro-lenses, along with a comparison to a bare, flat silicon wafer (with unmodified surface). First, the surface reflection is reduced from 30% for a planar silicon surface to only 11% or 14% for the nano-patterned surfaces (due to improved impedance matching). Second, lens focusing power for this microlens should be characterized by two different parameters: distance to a plane of minimal spot size, and a distance to a plane with maximal power concentration within a smaller square (such as a quarter of the original square lens area). In particular, more than



one-third of the input beam power can be concentrated into a “half-pixel” size square,  $15\mu\text{m} \times 15\mu\text{m}$ , near the center of a beam passing through the lens. Meanwhile, peak intensity can be doubled (Fig. 9) at the plane of smallest spot size when compared to the flat silicon wafer. Focal distances observed for our 18 micro-lenses varied from about  $160\mu\text{m}$  (see Fig. 8), up to approximately half a millimeter,  $450\mu\text{m}$  and  $510\mu\text{m}$  for the two lenses with a circular and square design, respectively (as listed in Table 1). This variation is due to both the variety of lens designs tested, as well as to finite tolerance of manufacturing process used.

**Table 1. Lens Characteristics**

	Bare Si Wafer	Circular Design	Square Design
Front Surface Reflectivity	30%	11%	14%
Portion of Input Power in $15\mu\text{m} \times 15\mu\text{m}$ spot	17.5%	35%	35%
Distance ( $\mu\text{m}$ ) to the position with maximal concentration in $15\mu\text{m} \times 15\mu\text{m}$ spot	N/A	450	510
Focal distance defined by a minimal spot size	N/A	122	221

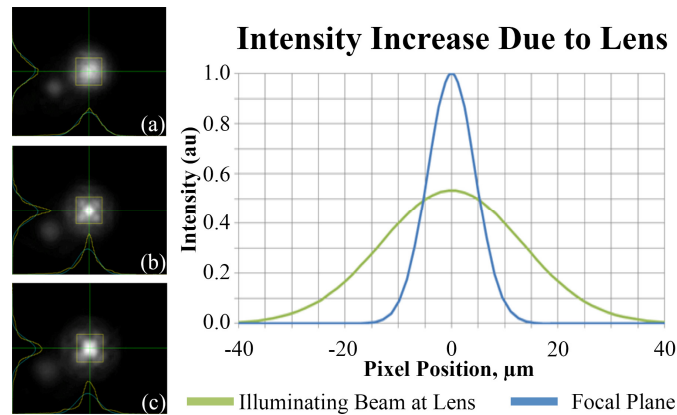


Fig. 9. The light intensity distribution at the micro-lens surface (a), at the minimal spot size (b), and at two focal lengths behind the focal plane (c). The yellow  $30 \times 30\mu\text{m}$  square represents the size of the original lens. Secondary reflection spots are visible near left lower corner of the photos. The intensity of the Gaussian beam at the micro-lens input (green) is compared to the measured intensity at the focusing plane (blue) for one of the micro-lenses (d).

## 7. Conclusion

In conclusion, we have demonstrated a sub-wavelength thin planar all-dielectric metamaterial lens patterned on a silicon wafer surface. A transparent dielectric substrate with no metal elements avoids light absorption as light passes through the metamaterial layer (in contrast to plasmonic meta-surfaces). One key advantage of this micro-lens design is a reduction in the insertion loss for wafer-level integrated micro-lenses down to about 10%, making this approach suitable for a variety of narrow-band and moderate bandwidth transmitting lens applications. Although the focusing surface layer was only about  $0.5\mu\text{m}$  thin, the resulting lens demonstrated a focusing distance of less than  $0.5\text{mm}$  with an attendant reduction in spot size by a factor of three. To design such lenses, we have created a parametric computer model that can calculate the phase of a plane wave passing through pillar structures of varying geometric parameters (including height, slope and diameter). These computer simulations show close correspondence with experimental measurements on fabricated structures.

## **Acknowledgments**

Authors are grateful to John Zolper, Srinivasiengar Govind, Roberta Gotfried, and Mark Skidmore for the project support. We would also like to express our thanks to the reviewers for their valuable comments and for bringing our attention to Ref. [31], which has not been available at the time of submission. This work was also supported in part by U.S. Army Research Office (ARO) grant 63133-PH (W911NF-13-1-0226), ARO Multidisciplinary University Research Initiative (MURI) grant #56154-PH-MUR (W911NF-09-1-0539), and Air Force Office of Scientific Research (AFOSR) MURI grant “Active Metasurfaces for Advanced Wavefront Engineering and Waveguiding”.